



## Original paper

# Monte Carlo and experimental evaluation of a Timepix4 compact gamma camera for coded aperture nuclear medicine imaging with depth resolution

Laura Antonia Cerbone<sup>a,c,f,5,\*</sup>, Luigi Cimmino<sup>b,c</sup>, Antonio Sarno<sup>b,c,1</sup>, Nicolò Vladi Biesuz<sup>d,e</sup>, Riccardo Bolzonella<sup>d,e</sup>, Giovanni Mettivier<sup>b,c,2</sup>, Massimiliano Fiorini<sup>d,e,3</sup>, Paolo Russo<sup>b,c,4</sup>

<sup>a</sup> Scuola Superiore Meridionale, Largo San Marcellino 10, 80138, Napoli, Italy

<sup>b</sup> Dipartimento di Fisica "Ettore Pancini", Università di Napoli Federico II, I-80126 Napoli, Italy

<sup>c</sup> Istituto Nazionale di Fisica Nucleare (INFN), Sezione di Napoli, I-80126 Napoli, Italy

<sup>d</sup> Dipartimento di Fisica e Scienze della Terra, Università di Ferrara, I-44122 Ferrara, Italy

<sup>e</sup> Istituto Nazionale di Fisica Nucleare (INFN), Sezione di Ferrara, I-44122 Ferrara, Italy

<sup>f</sup> Università di Napoli Federico II, 80138, Napoli, Italy

## ARTICLE INFO

## Keywords:

Compact gamma camera

Timepix4

Geant4

Monte Carlo simulation

CdTe

Coded aperture imaging

## ABSTRACT

**Purpose:** We designed a prototype compact gamma camera (MediPROBE4) for nuclear medicine tasks, including radio-guided surgery and sentinel lymph node imaging with a <sup>99m</sup>Tc radiotracer. We performed Monte Carlo (MC) simulations for image performance assessment, and first spectroscopic imaging tests with a 300 μm thick silicon detector.

**Methods:** The hand-held camera (1 kg weight) is based on a Timepix4 readout circuit for photon-counting, energy-sensitive, hybrid pixel detectors (24.6 × 28.2 mm<sup>2</sup> sensitive area, 55 μm pixel pitch), developed by the Medipix4 Collaboration. The camera design adopts a CdTe detector (1 or 2 mm thick) bump-bonded to a Timepix4 readout chip and a coded aperture collimator with 0.25 mm diameter round holes made of 3D printed 1-mm thick tungsten. Image reconstruction is performed via autocorrelation deconvolution.

**Results:** Geant4 MC simulations showed that, for a <sup>99m</sup>Tc source in air, at 50 mm source-collimator distance, the estimated collimator sensitivity ( $4 \times 10^{-4}$ ) is 292 times larger than that of a single hole in the mask; the system sensitivity is 0.22 cps/kBq (2 mm CdTe); the lateral spatial resolution is 1.7 mm FWHM. The estimated axial longitudinal resolution is 8.2 mm FWHM at 40 mm distance. First experimental tests with a 300 μm thick Silicon pixel detector bump-bonded to a Timepix4 chip and a high-resolution coded aperture collimator showed time-over-threshold and time-of-arrival capabilities with <sup>241</sup>Am and <sup>133</sup>Ba gamma-ray sources.

**Conclusions:** MC simulations and validation lab tests showed the expected performance of the MediPROBE4 compact gamma camera for gamma-ray 3D imaging.

## 1. Introduction

A compact gamma camera (CGC) is a lightweight, small field of view, hand-held, gamma-ray imaging device that can be used for pre- and intra-operative clinical procedures in nuclear medicine, typically employing <sup>99m</sup>Tc radiotracers [1,2]. These include sentinel lymph node (SLN) scintigraphy and radio-guided surgery [3,4]. CGCs are based on a

monolithic or pixelated scintillator crystal detector, or on a pixel semiconductor detector: two technologies with distinctive advantages and drawbacks [5]. In scintillator-based CGCs, each gamma-ray interacts with a thick scintillator crystal and produces a light pulse of thousands of optical photons, whose spatial distribution and intensity is read-out by a 2D optical detector (position-sensitive photomultiplier tube, array of photodiodes or silicon photomultipliers).

\* Corresponding author.

E-mail address: [lauraantonia.cerbone-ssm@unina.it](mailto:lauraantonia.cerbone-ssm@unina.it) (L.A. Cerbone).

<sup>1</sup> ORCID: 0000-0002-3034-7166

<sup>2</sup> ORCID: 0000-0001-6606-4304

<sup>3</sup> ORCID: 0000-0001-6559-2084

<sup>4</sup> ORCID: 0000-0001-9409-0008

<sup>5</sup> ORCID: 0000-0002-9449-9927

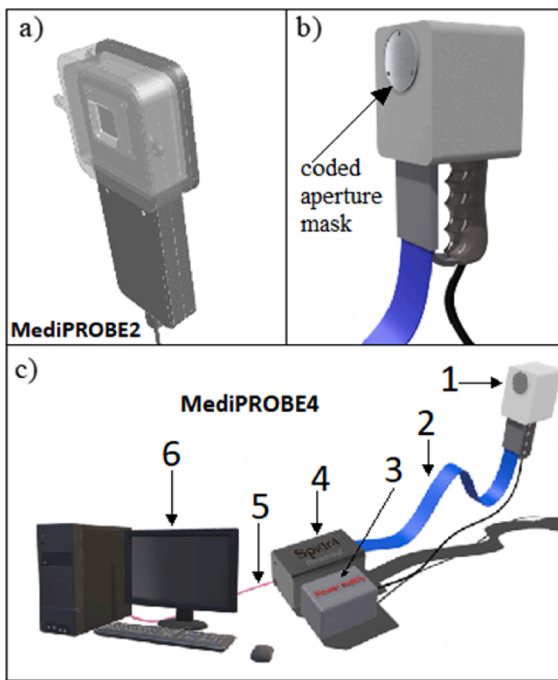


**Fig. 1.** a) CAD view of the MediPROBE2 CGC (2011), adopting a Medipix2 readout chip bump-bonded to a 1-mm thick CdTe detector and a pinhole collimator; b) 3D model of the MediPROBE4 CGC (2022) adopting a Timepix4 readout chip, a 2-mm thick CdTe detector and a coded aperture mask, which can be rotated in place for correct alignment with the Timepix4 sensor array. c) MediPROBE4 acquisition system: 1. MediPROBE4 camera head; 2. Flat cable; 3. Sensor and chip power supply; 4. SPIDR4 readout electronics; 5. Optical fiber fast link connection (10 gbps, 3 m length); 6. Personal computer with a PCIe board type 2-port SFP + 10GbE Standard LP with SFP + connectors.

In semiconductor-based CGCs, gamma-rays interact directly with a semiconductor crystal (e.g., Si, CdZnTe, CdTe, with thickness from 0.3 mm to a few mm) and produce thousands of electron-hole pairs. Electrons and holes are separated by an intense electric field due to an applied voltage bias between the two sides of the pixel detector (tens to a few hundred volts) and migrate toward corresponding electrodes. The charge (electrons or holes) is then collected at the pixel electrode, which is connected via bump-bonding to the corresponding pixel cell electronics of the readout chip. This charge produces a signal via a charge-sensitive preamplifier, with a pulse height proportional to the charge and, hence, to the photon energy deposited in that pixel cell. The readout circuit for each pixel can be based on the photon counting technology (i.e., a hit is recorded if the charge signal is above a threshold), as well as on the energy selective technology (i.e., the energy deposited by each photon interacting in the pixel is measured and recorded).

### 1.1. Medipix and Timepix readout circuits

Working within a European collaboration based at CERN ([www.cern.ch/medipix](http://www.cern.ch/medipix)), our group developed radiation imaging devices for electron imaging [6], for positron imaging [7] and gamma-ray imaging [8–10] using hybrid pixel detectors of the Medipix series, that are based on the semiconductor technology we discussed above.

A hybrid pixel detector is an assembly composed of a semiconductor (e.g., Si, GaAs, CdTe, CdZnTe) pixel detector connected electrically, pixel-by-pixel, via bump-bonding, to a readout application-specific integrated circuit (ASIC), whose array of identical microelectronic cells has the same geometry as the 2D array of detector pixels. A first CGC was developed in 2002 for sentinel lymph node imaging [11,12] using low-detection efficiency silicon pixel detectors bump-bonded to a Medipix1 photon counting ASIC, featuring  $64 \times 64$  pixels with  $170 \mu\text{m}$  pitch. With

the availability of the Medipix2 photon counting ASIC and Timepix2 energy selective ASIC ( $256 \times 256$  pixels with  $55 \mu\text{m}$  pitch), and efficient 1-mm thick CdTe pixel detectors [13,14], a prototype CGC (MediPROBE) was assembled, here referred to as MediPROBE2, since it was based on the Medipix2 or Timepix2 ASICs, as summarized below.

### 1.2. MediPROBE2 compact gamma camera

MediPROBE2 [14] was a CGC based on a 1-mm thick CdTe semiconductor hybrid pixel detector (sensitive area  $14.08 \times 14.08 \text{ mm}^2$ ) electrically connected pixel-by-pixel to the Medipix2, or to the Timepix2, photon counting CMOS ASICs [15] (Fig. 1a). This imaging device was operated at a single low-energy threshold (5 keV), and it was equipped with a set of interchangeable tungsten knife-edge pinhole collimators (hole aperture diameter 0.35 mm, 0.94 mm or 2.1 mm). This CGC – developed for nuclear imaging with  $^{99\text{m}}\text{Tc}$  radiotracers and thyroid imaging – showed good performance for both point-like sources [16] and lymph node imaging [14].

During clinical tests for SLN imaging, MediPROBE2 was operated using a single pinhole collimator: for a fixed detector-collimator distance (10 mm), the camera had a variable field of view (FOV) in dependence of the source-collimator distance. A typical FOV was  $40 \times 40 \text{ mm}^2$  at 50 mm source-collimator distance, corresponding to a minification factor 5:1. For  $^{99\text{m}}\text{Tc}$ , at 50 mm source-collimator distance, MediPROBE2 featured a background-subtracted system sensitivity of  $6.5 \times 10^{-3} \text{ cps/kBq}$  and a spatial resolution of 5.5 mm FWHM (0.94 mm pinhole collimator). Corresponding values for the 2.1 mm pinhole were  $3.3 \times 10^{-2} \text{ cps/kBq}$  and 12.6 mm FWHM, respectively. We later equipped MediPROBE2 with two interchangeable coded aperture (CA) masks [16] (no-two-holes-touching modified uniformly redundant array NHTT MURA  $62 \times 62$ , 480 holes in the central pattern, 12.5% open fraction,  $70 \mu\text{m}$  or  $80 \mu\text{m}$  hole aperture, made of pure tungsten, 100 or 110  $\mu\text{m}$  thick, respectively), initially designed for  $^{125}\text{I}$  low-energy gamma-ray high-resolution imaging in small animals [17,18].

CA masks are multi-aperture collimators with hundreds of apertures arranged in a specific 2D pattern, whose geometrical efficiency is high thanks to the presence of many holes, and whose spatial resolution is that of a single aperture in the mask. This comes at the expense of partial multiplexing of the images produced by the apertures; a post-acquisition image reconstruction process returns the final image for display. While the detector's plane distance from the mask is fixed, the longitudinal distance of the radioactive source plane is a free parameter: the computational reconstruction procedure can therefore be repeated at several distances. This technique (laminography) [19–22] permits adding (longitudinal) depth resolution to the 2D imaging performance of the CGC.

Previously, via experimental tests using MediPROBE2 equipped with these CA masks [16] and a Timepix2 ASIC, we showed a lateral spatial resolution of 0.64 mm FWHM and 3 mm FWHM longitudinal resolution (60 keV, 50 mm source-collimator distance,  $40 \times 40 \text{ mm}^2$  FOV, 1-mm CdTe detector). X-ray sources were also imaged with high resolution using the same CA masks [23].

### 1.3. MediPROBE4 compact gamma camera

In this work, we evaluated the performance of a new design of MediPROBE CGCs (MediPROBE4), via Monte Carlo (MC) simulations. We also reported the first experimental tests on the MediPROBE4 semiconductor-based CGC, which utilizes the new Timepix4 readout ASIC and a high-resolution coded aperture collimator. The performance of MediPROBE4 was analysed also with respect to MediPROBE2 [14].

We note that, while the laboratory measurements were carried out only with a prototype Timepix4 assembly featuring a 300  $\mu\text{m}$  thick Si pixel detector (the only version available at present), the MC simulations here reported referred also to the future version of a Timepix4 ASIC bump-bonded to a CdTe detector, which will be employed in the final

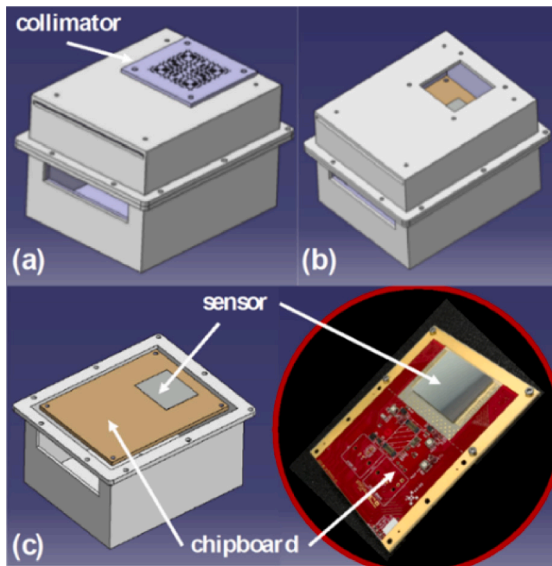


**Fig. 2.** 3D model of the detector chipboard and housing (top and bottom parts assembled). 3D view of the box with (a) or without (b) the collimator in place. c) View of the bottom part, hosting the chipboard and the detector. d) Photo of the Timepix4v1 detector used in this work (bonded to a 300  $\mu\text{m}$  thick Si sensor array).

version of MediPROBE4 but is still unavailable. With the availability of a larger ASIC (about 7  $\text{cm}^2$  for Timepix4, with respect to about 2  $\text{cm}^2$  for Timepix2 and Medipix2 ASICs), in MediPROBE4 it was possible to obtain a larger FOV at a given source-collimator distance, with respect to MediPROBE2. Since a large imaging FOV coupled to a high sensitivity was the main design goal for MediPROBE4, in the present setup, we accepted a lower spatial resolution of MediPROBE4 with respect to MediPROBE2 equipped with a CA mask. Yet, in the present design, the calculated lateral resolution was good enough for the imaging tasks of such a CGC, while the FOV was significantly larger than most CGCs that we analysed for comparison.

In the image reconstruction (decoding) process, the position of the source in the object plane is not known *a priori* and can be verified *a posteriori* via decoding at various distances and then selecting the “best focus” distance of the object plane. This motivates the various simulation tests here shown, to check the performance of the decoding process, whose properties are separated from the properties of the optical (CA mask) system. A different decoding algorithm produces different images with different image quality. All simulations and experiments were carried out at source distances of a few cm from the collimator, as expected in the case of SLN localization tasks.

## 2. Materials and methods

### 2.1. Timepix4 readout ASIC

Timepix4 [24,25] is a hybrid pixel detector readout ASIC that is part of the Medipix/Timepix family, developed at CERN by the Medipix collaboration for a wide range of applications, from high energy physics to electron spectroscopy, to medical physics [26]. The Timepix family differs from the Medipix ASIC series for its capability to measure the time of arrival of ionizing particles (*ToA*), as well as to record, correspondingly, the time during which the charge deposited in a pixel is over a pre-set threshold (*ToT*), hence enabling the determination of the energy of the interacting particle for each pixel. The Timepix4 ASIC contains  $448 \times 512$  square cells for pixel signal processing, and it is designed to be connected to a pixelated semiconductor sensor consisting of  $448 \times 512$  square pixels with a pitch of 55  $\mu\text{m}$ , corresponding to a sensitive area of 694  $\text{mm}^2$  ( $24.6 \times 28.2 \text{ mm}^2$ ). Timepix4 top surface

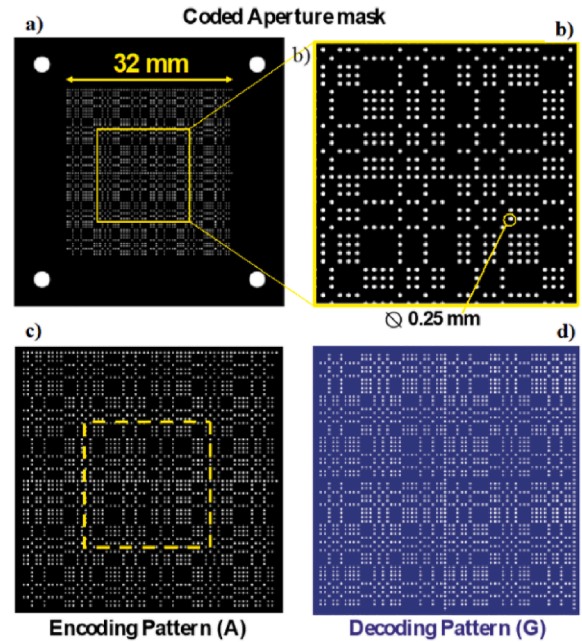


**Fig. 3.** a), b) Coded aperture collimator (mura mask, rank 31, holes of 0.250 mm diameter; material: pure Tungsten, 1 mm thick. c) Encoding and d) ideal decoding pattern of the CA mask; for MURA masks, the correlation between these two gives a delta function. This peculiarity allows to reduce the intrinsic noise in the decoded image. The pattern displayed (with white circles representing holes in the otherwise solid sheet of material in black) corresponds to the antisymmetric MURA mask (rank 31) adopted in this work, made of pure tungsten, and containing a central array of 480 round holes (highlighted in the yellow square) cyclically replicated on the four sides for the fourfold larger coded array physically used for imaging.

comprises a matrix of  $448 \times 512$  bonding pads, to which the sensor (a Silicon pixel detector of 300  $\mu\text{m}$  thickness, in this work, or a CdTe sensor, in the future) is connected via bump-bonding to each corresponding pixel electrode in the matrix array. The top electrode of the sensor is a (guard-ringed) uniform electrode. This readout ASIC can operate in Frame-Based mode – photon counting – and Data-Driven mode. The latter (adopted here) allows to perform measurements with *ToT* and *ToA*, thus enabling particle tracking and spectral imaging.

### 2.2. MediPROBE4 layout

MediPROBE4 CGC can be used for pre- and intra-operative procedures. This device's working system scheme is shown in Fig. 1b,c.

The camera head is connected through a semi-rigid flat cable to a control board and readout system (Spidr4) developed by a group at Nikhef [27]. The output is transmitted via 2 serializers working at a bandwidth of 40 Mbps, or 16 serializer that can potentially reach a bandwidth of 10 Gbps. A 3D-printed ABS box of size  $94 \times 114 \times 72 \text{ mm}^3$  houses the chipboard with its connectors and cables (Fig. 2).

Adjustable internal supports hold up the chipboard and allow the regulation of collimator-to-detector distance as needed. The flat cable connecting to the Spidr4 data readout system, the Timepix4 power supply line and the CdTe detector voltage bias supply line, come out from the bottom of the box. A 3D-printed removable ergonomic handle is connected to the box for manual operation, but using a robotized arm is possible (as for MediPROBE2). The external shell is shielded with 2-mm thick lead foils, covering the entire box, except for the two apertures for the collimator and the wires. The shielding weight is approximately 0.8 kg, while the weight of the whole device is about 1 kg.



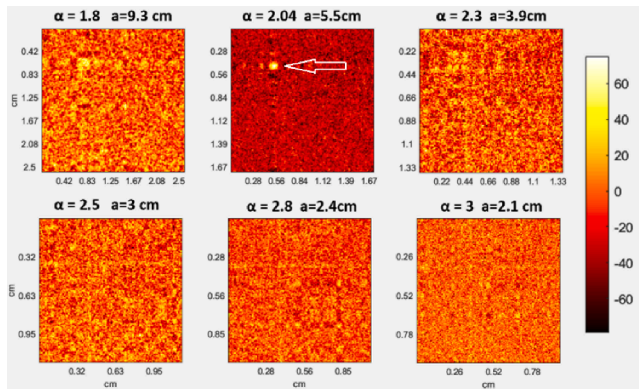


**Fig. 4.** Output images from the reconstruction process, for an off-axis point-like  $^{99m}\text{Tc}$  simulated source. Six false-color images are shown, corresponding to  $n = 6$  reconstruction object planes (at various distances, indicated as  $a$ ). The parameter  $\alpha$  indicated on the panels is the fractional number of sensor pixels in the image plane covered by the projection of a single hole in the CA mask, while  $a$  is the distance of the reconstruction plane from the collimator. The source can be identified as the yellow spot in the upper left corner (indicated by the white arrow in the in-focus image). The “best focus” reconstruction plane was selected either visually or by CNR analysis. In the case of single or multiple sources extending in the axial direction, this reconstruction process (laminography) permits to return the lateral distribution of the source activity as well as the axial extension and position of the source(s).

**Table 1**

Input parameters for the Matlab image reconstruction code.

Parameter	Symbol
Number of pixel positions (open or closed) in one period of the coded mask	$npm$
Hole aperture diameter	$d$
Number of pixels of the detector	$npix$
Detector's pixel dimension	$dp$
Reconstruction distance from the mask	$a$
Fraction of projected pixels per aperture	$\alpha$
Numbers of object planes for reconstruction	$n$

### 2.3. Coded aperture collimator

The collimator for MediPROBE4 was a centrally anti-symmetric CA collimator, NTH 62  $\times$  62 MURA mask, mosaicked, pattern centered (Fig. 3a,b), which can be represented numerically by a binary matrix,  $A(i,j)$ , containing either 0 (for a hole in the mask) or 1 (for an opaque part). The design of this CA mask was of the same type as the one adopted for MediPROBE2, but we adopted a larger size of the apertures for increasing the collimator sensitivity, and a greater thickness for decreasing the transmission of radio-opaque areas. The pure tungsten mask's parameters (hole diameter and length) were optimized via MC simulations in the trade-off between low transmission and high geometric efficiency, for a final configuration of a 1-mm-thick mask with 0.25 mm diameter round holes.

### 2.4. Reconstruction software

Images acquired with CA masks undergo a decoding process to reconstruct the 3D radioactivity distribution in the object space (Fig. 4).

This can be done using several algorithms; in our case, decoding was realized using a MURA periodic correlation decoding algorithm [17,18] based on the deconvolution (correlator operator,  $\otimes$ ) between the acquired image matrix  $I(i,j)$  and a 2D decoding pattern,  $G(i,j)$ , such that once correlated with the mask matrix, it returns the 2D delta function:  $A \otimes G = \delta$ . In the reconstruction (i.e., decoding) process, we adopted an off-line Matlab code, in which we input values for the parameters

**Table 2**

Characteristics of the CA mask used in the experimental setup compared to those of the simulated CA mask.

Parameter	Simulated CA mask	Experimental CA mask
Aperture diameter (mm)	0.25	0.080
Collimator thickness (mm)	1	0.11
Material	W	W
Aperture acceptance angle ( $^\circ$ )	28	180
No. of apertures	480	480

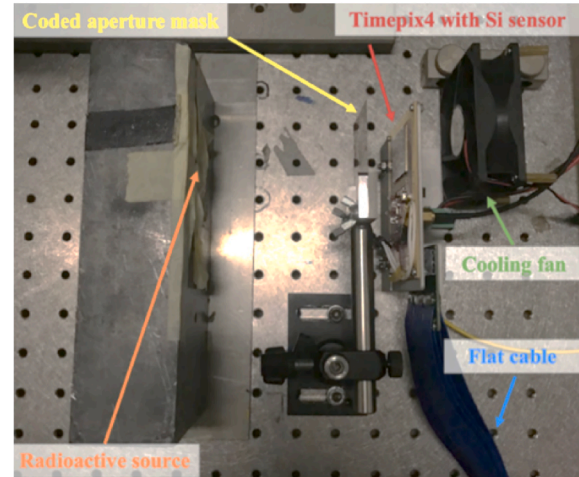


**Fig. 5.** Experimental set-up for testing Timepix4 equipped with a coded aperture mask. The mask was placed in front of the sensor at 22 mm. The radioactive source was placed at various distances from the mask to test its capability of reconstructing images of the object for different planes.

**Table 3**

Test conditions used for the Timepix4/collimator system.

Radioactive source	Activity (kBq)	Collimator to detector distance (mm)	Source to collimator distance (mm)	Acq. time (s)
$^{133}\text{Ba}$	250	22	62	10,800
$^{241}\text{Am}$	336	22	96	4920

reported in Table 1. Image reconstruction is then carried out at various distances,  $a$ , from the collimator face, with visual choice of the in-focus image (Fig. 4); focusing was also carried out off-line via calculation of image contrast-to-noise ratio (CNR) of visible sources.

### 2.5. Timepix4 experimental tests with radioactive sources

Laboratory tests for spectral imaging of radioactive sources were carried out using a CA mask available in the laboratory (Table 2) and a prototype version of the Timepix4 ASIC bump bonded to a 300  $\mu\text{m}$  thick silicon sensor with 448  $\times$  512 pixels, 55  $\mu\text{m}$  pitch. The readout system to stream and collect data from the chip is the Spidr4 hardware, developed by Nikhef Institute (partners of the Medipix4 collaboration), with its in-house software. A photo of the experimental setup is shown in Fig. 5.

The Timepix4 ASIC was operated in Data-Driven mode with a minimum detection threshold set to 1500 electrons and a shutter time of 30 s per image, using a  $^{133}\text{Ba}$  and  $^{241}\text{Am}$  gamma-ray sources. After each acquisition, data was stored, the chipboard was reset, and a new image was acquired, for a sequence of successive acquisitions up to 2 h long; Table 3 shows the acquisition parameters. The long exposure time is due to the low activity of the source, while repeated measurements helped mitigate instabilities in the ASIC prototype.



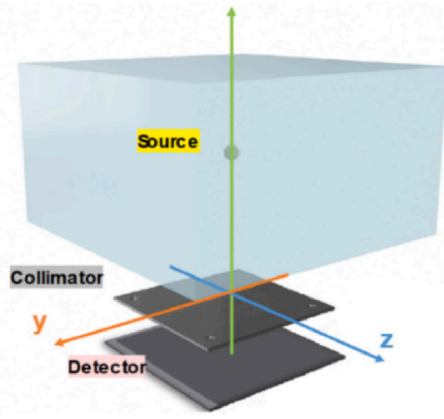


**Fig. 6.** Set-up scheme used for both Monte Carlo simulations and tests of the Timepix4-based MediPROBE4 with a spherical radioactive source. The source was either air or immersed in a water box, with or without background activity distributed uniformly in the box.

## 2.6. Image processing and analysis

Images obtained from the experimental test were processed using a software developed with the Root toolkit to analyze data collected by Timepix4 ASICs [29]. This software performs a preliminary cleaning consisting of counting the number of hits in a single pixel and removing all the hits detected in “noisy” pixels (i.e., pixels counting the number of hits above a predefined threshold). A finer cleaning can be realized by exploiting the clustering algorithm. This recognizes spatial clusters (i.e., composed of almost simultaneous hits), associated with a single interacting particle; noisy clusters (i.e., several hits in the same pixel with different, but close enough, *ToA* values), associated with noisy pixels; and point clusters, i.e., hits isolated from all the others (not detected as noisy neither spatial). Due to the initial stage of development of this software, no energy calibration was possible; hence the actual information on the energy of photons interacting in the sensor is still unavailable. Nevertheless, since – apart from low energies close to the threshold – energy deposition is proportional to *ToT*, this last can be used to set the detection threshold and to recognize detected photons of the same energy. A *ToT* range selection was applied for energy centering around the source’s emission line(s).

## 2.7. MC simulations and experimental validation

MC simulations were carried out using the toolkit Geant4 [28] Version 10.6 with the physics list Option4. The geometrical configuration used for the simulations is shown in Fig. 6.

For the assessment of MediPROBE4 performance, the collimator-detector distance was fixed at 10 mm (from the lower surface of the mask to the upper surface of the detector), while the source-collimator distance was changed as required in the various tests. The simulated sensor is made of a 1-mm or 2-mm thick slab of CdTe (density, 5.8 g/cm<sup>3</sup>) divided into 800 × 800 square pixels, each 55 μm by side. Within the sensor, photoelectric absorption, coherent and incoherent scatter, and de-excitation processes were simulated and the energy deposition within each pixel was scored (electron range cut-off set to 1 μm). This information was eventually used to assess the detection efficiency and estimate the system sensitivity. X-ray fluorescence events in the collimator and in the detector were simulated as well.

The simulated photon source was either a point-like, a circular planar, or a spherical source. The diameter of the extended sources was varied in a series of simulations, to investigate the effect of increasing FOV coverage on the imaging performance of the CA mask. For the point source, its lateral position was varied to determine the extent of the imaging FOV, at the given reconstruction distance from the collimator. A

<sup>99m</sup>Tc radioactive source was simulated as a monoenergetic source emitting gamma-rays of 140.5 keV. Photons were emitted from each point of the source within a cone whose angular opening was chosen to cover the whole detector. The number of photon histories run in each simulation was 10<sup>7</sup>, unless otherwise stated. Decoded image quality was assessed in regions of interest (ROIs) on reconstructed images showing the source and the background, via calculation of CNR from the mean value  $\mu$ , and standard deviations  $\sigma$ , in the ROIs, as follows:

$$CNR = \frac{\mu_{source} - \mu_{bkg}}{\sigma_{bkg}}. \quad (1)$$

The diameter of the ROIs was chosen accordingly to the extension of the source in each image: this was evaluated from the FWHM of the peak in a line profile across the source.

To benchmark our simulation platform, we reproduced the experimental set-up used to acquire the image of the radioactive sources we used. In the case of the <sup>133</sup>Ba source, we simulated a point-like, monoenergetic source emitting photons of 30.85 keV onto the sensor. The number of simulated histories (2 × 10<sup>6</sup>) was chosen to reproduce the activity of the source used in the experimental test. The source was placed at 63 mm from the collimator, and at 5 mm – in both the *x* and *y* direction – from the collimator axis. We simulated a 300 μm thick Silicon sensor with a matrix array of 512 × 448 square pixels of 55 μm side. We also simulated the CA MURA mask used for the experimental tests (0.08 mm holes, 0.11 mm thick), placed at 22 mm from the sensor. Corresponding raw images were decoded with the reconstruction software, using the same parameters chosen for the experimental tests.

The same procedure was repeated for the <sup>241</sup>Am source: the source was simulated as a monoenergetic (59.5 keV photons) point-like source placed at 96 mm from the mask (in the *z* direction), at 3 mm in the *x* direction and 5 mm in the *y* direction with respect to the center of the FOV. We must point out that in this Monte Carlo platform the charge sharing between pixels of the detector was not simulated, as we did not reproduce neither the charge collection nor the bias voltage applied to the sensor. We only evaluated the energy released in each pixel by interacting photons.

## 2.8. Field-of-view, lateral spatial resolution, axial spatial resolution and sensitivity of MediPROBE4

The calculated field of view (FOV) of the CA mask [22] was 90.3 × 90.3 mm<sup>2</sup>, at a source to collimator distance of 50 mm, for a fixed collimator-detector distance of 10 mm. The extent of the FOV was also assessed by simulating a point-like source (<sup>99m</sup>Tc) placed at increasing lateral distances from the collimator axis and analysing the resulting decoded images. The lateral spatial resolution of the collimator (i.e., in planes parallel to the collimator plane) was assessed by analysing the source profile in the decoded image of a point-like source (approximately 0.5 mm in diameter) placed on-axis at 50 mm from the collimator face. The estimated axial spatial resolution in the 3D reconstruction of the source position – that is, the depth resolution in the longitudinal direction normal to the collimator plane – was obtained as the FWHM of the measured point-like source profile obtained by simulating two point-like <sup>99m</sup>Tc sources at different axial distances from the collimator face.

MC simulations were carried out also for extended <sup>99m</sup>Tc sources. A spherical source, with 10 mm diameter and emitting 10<sup>7</sup> photons, was located on-axis at 50 mm from the collimator, immersed in a water box (90 × 90 × 50 mm<sup>3</sup>) for simulating the surrounding soft tissue (Fig. 6). A background activity was simulated in the water box (3 × 10<sup>8</sup> photons uniformly distributed within the box) with a source-to-background activity ratio (SBR) of 26:1, computed as follows:

$$SBR = \frac{\frac{\#photons\ emitted\ by\ the\ source}{source\ volume}}{\frac{\#photons\ emitted\ by\ the\ box}{water\ box\ volume}}. \quad (2)$$

In this case, a 448 × 512 pixels sensor was simulated. The detection

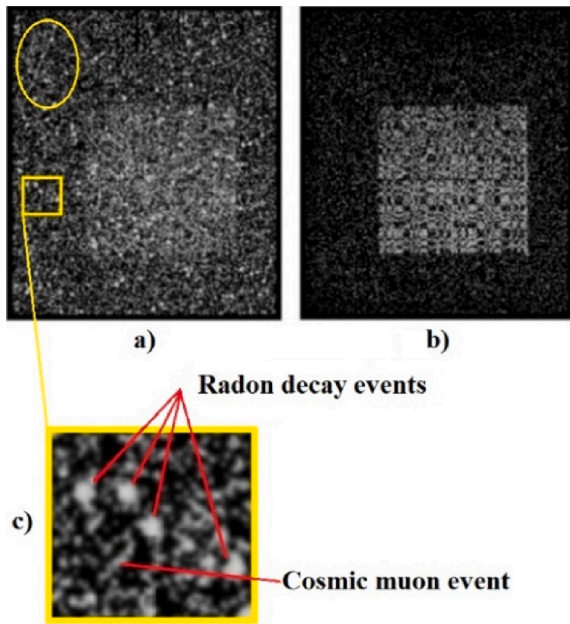


**Fig. 7.** a) Experimental raw image of a point-like  $^{133}\text{Ba}$  radioactive source at 62 mm from the collimator, acquired with a Timepix4 ASIC bump-bonded to a 300  $\mu\text{m}$  thick Si detector, using a CA mask with 80  $\mu\text{m}$  hole apertures (Table 2). b) Processed image, after performing a *ToT* selection and a cleaning procedure using clustering software to remove non-point-like clusters. c) Zoomed image of the rectangle highlighted in yellow in (a), showing pixel hits corresponding to particle tracks of detected Radon decay single events (“blobs”, almost round pixel clusters), and energetic cosmic ray muons (straight tracks of several pixels length). Low-energy photons emitted by the  $^{133}\text{Ba}$  source produce mostly single-pixel hits. A several-mm long muon track is visible in the upper left corner of the image in (a), encircled in yellow.

efficiency of the sensor, i.e., energy deposition within the sensor, was not considered for these simulations (i.e., the energy-resolved photon fluence per pixel on the detector surface was scored). The overall geometrical sensitivity of the CGC is given by the product of the fraction of the total solid angle subtended by the detector, and the geometric efficiency of the collimator. For a point-like source, the former term is inversely proportional to the square of the axial source-detector distance.

MC simulations were carried out to estimate the second term. To study the (on-axis) collimator sensitivity, Geant4 simulations were performed using point-like sources placed at the center of the mask at different axial distances from the collimator surface. The number of photons incident on the detector surface was kept fixed for all these simulations. The same simulations were carried out, substituting the coded aperture collimator with a solid tungsten plate of 1 mm thickness and for a single, round, channel pinhole with a diameter of 0.25 mm, to simulate the response of a single aperture in the mask. For a fixed number of photons arriving on the collimator, we hence scored the number of photons passing through the coded mask, then through a single hole in the mask, and the number of photons transmitted by the solid (no openings) 1-mm thick tungsten plate. We then determined the background subtracted sensitivity for both the pinhole collimator and the CA mask, using the following formula:

$$g = \frac{\# \text{photons through apertures} - \# \text{photons through W slab}}{\# \text{photons arriving at the collimator surface}} \quad (3)$$

The system sensitivity of the (energy-selective) CGC (detected count rate per unit activity) is the product of geometrical sensitivity (fraction of emitted gamma-rays arriving at the detector surface) and intrinsic (detection) efficiency (evaluated as the fraction of gamma-rays incident on the detector that is detected under the full-energy spectral peak). MC simulations were carried out to also estimate the detection efficiency of

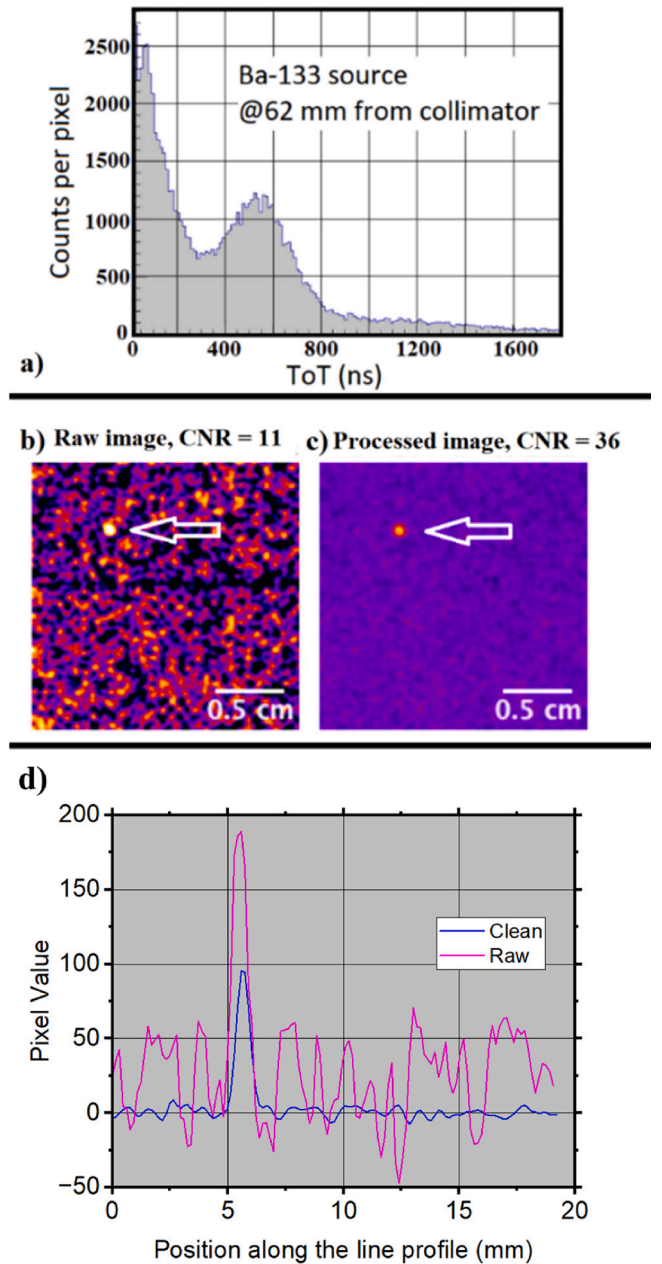


**Fig. 8.** a) Histogram of the *ToT* of the events for a  $^{133}\text{Ba}$  source placed at 62 mm from the collimator. b) Reconstructed image of the  $^{133}\text{Ba}$  source, after applying a Gaussian filter ( $\sigma = 1$  pixel). The white arrow indicates the source. c) Reconstructed image of the  $^{133}\text{Ba}$  source after applying the *ToT* selection and a Gaussian spatial filter ( $\sigma = 1$  pixel). d) *ToT* windowing permitted to increase the CNR (by 92%), as also evident from a line profile across the source image.

the CdTe detector. This was obtained by simulating a monoenergetic source emitting photons of 140.5 keV onto a 1 mm thick CdTe detector first, and a 2 mm thick CdTe detector later. For each photon impinging on the detector, we scored the energy released in a detector pixel, with a minimum threshold of 60 keV for counting a hit.

### 3. Results

#### 3.1. Experimental tests and MC simulation for a $^{133}\text{Ba}$ source

Laboratory tests were carried out with gamma-emitting  $^{133}\text{Ba}$  and  $^{241}\text{Am}$  radioactive sources. Fig. 7 shows the acquired image (a) and post-

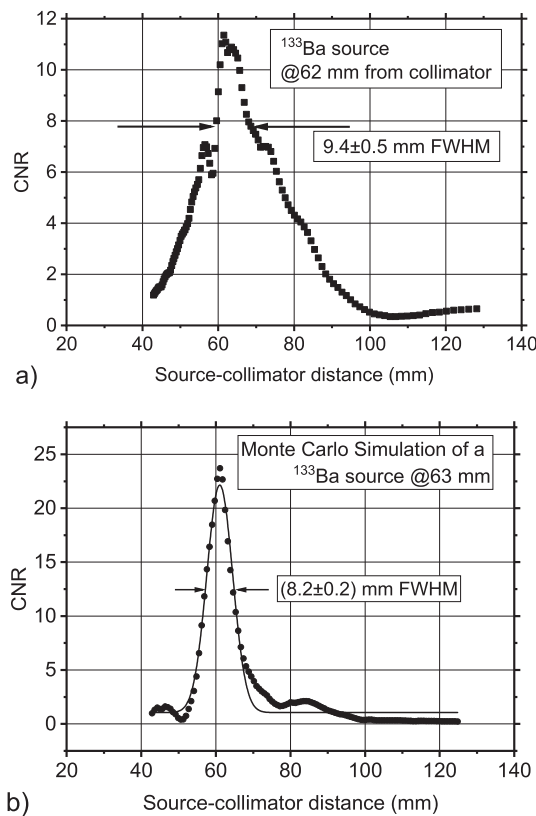


**Fig. 9.** a) CNR of the source image evaluated at many successive reconstruction planes as a function of the distance from the collimator, for a  $^{133}\text{Ba}$  source placed at 62 mm from the collimator face. The source-detector distance was 22 mm. A Gaussian fit on the source peak longitudinal profile (not shown) indicated an axial spatial resolution of 9.4 mm FWHM. Measurements were carried out with Timepix4 bonded to a 300  $\mu\text{m}$  thick Si detector. b) CNR as a function of the source-collimator distance for the MC; a Gaussian fit indicated an axial spatial resolution of 8.2 mm FWHM.

processed image (*ToT* and cluster analysis) obtained using a  $^{133}\text{Ba}$  source (about 1 mm diameter), placed 62 mm from the CA collimator. The Timepix4v1 ASIC was coupled to a 300  $\mu\text{m}$  thick Si sensor, having negligible detection efficiency for 81 keV and 356 keV photons emitted by the  $^{133}\text{Ba}$  source. On the other hand, 30.85 keV photons emitted by this source have a significant probability (about 90%) of interacting in this sensor. In the acquired image in Fig. 7a (post-processed in Fig. 7b), the shadow of the mask pattern is barely visible due to the noise given by alpha particles emitted by Radon decay in air (visible as large white blobs), and by cosmic rays (straight tracks), which easily penetrate the collimator foil (0.11 mm tungsten) (Fig. 7c).

Fig. 8a shows the histogram of *ToT* of events detected by the Timepix4 detector. A peak centered around 575 ns can be noticed: from the dependence of *ToT* on photon energy, we attributed the events under this peak to the detection of 30.85 keV photons emitted by  $^{133}\text{Ba}$ . Hence, we applied a *ToT* windowing procedure by selecting detector hits whose *ToT* value was between 400 ns and 700 ns. Fig. 8b shows the decoded image obtained from acquired data, while Fig. 8c shows the reconstructed image obtained by decoding the post-processed data and by applying the *ToT* (energy selection) procedure.

For the former image, the CNR is about 11, while for the latter, it is about 36 (Fig. 8d). These values quantify the improvement in the image quality deriving from the *ToT* selection and the cleaning procedure. From the post-processed acquisition, we reconstructed a 3D image of the source (laminography technique). Fig. 9 shows the CNR as a function of the distance of the reconstruction plane from the collimator face, for a  $^{133}\text{Ba}$  source (0.6 mm diameter) placed at 62 mm from the collimator face.

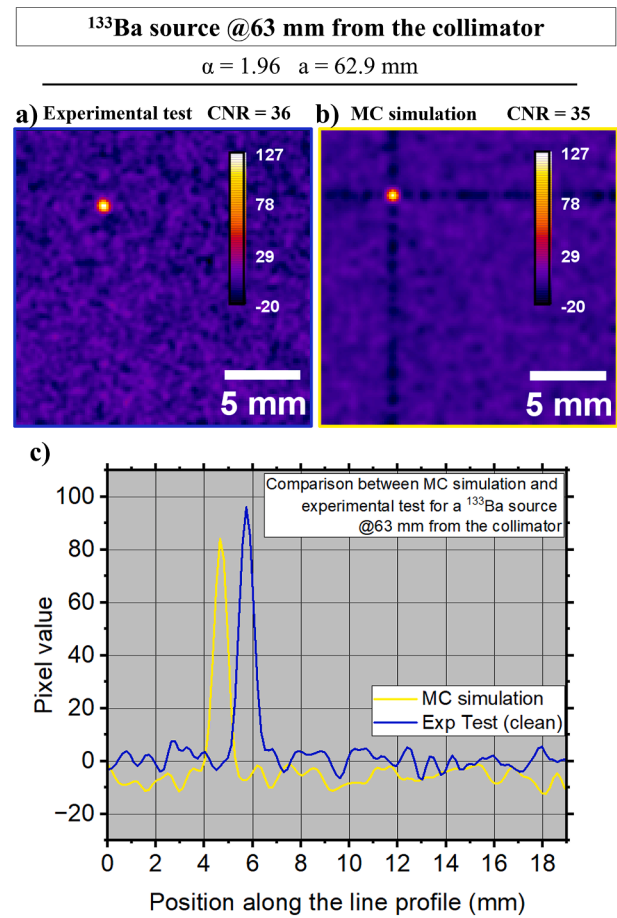


**Fig. 10.** a) Image of the  $^{133}\text{Ba}$  source (at 63 mm from the collimator) obtained from experimental tests. b) Reconstructed image of the simulated source (object plane at 62.9 mm). Images were decoded for a reconstruction plane placed at 62.9 mm from the collimator. c) Source profile for the measured and simulated images: the two profiles are in good agreement, except for a 1 mm shift in the lateral position, due to a slight displacement of the source with respect to the MC simulation.

In the reconstruction process, we assign the range of axial distances and the number of object planes for decoding the image of the source. As the reconstruction plane approaches the actual distance at which the source is placed, the CNR of the source increases, reaching a maximum.

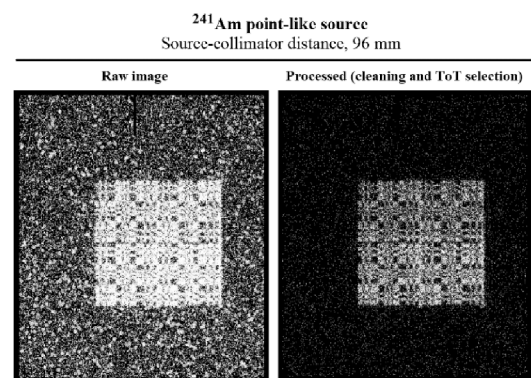


**Fig. 11.** a) Experimental detector image obtained with a point-like  $^{241}\text{Am}$  source at 96 mm from the collimator. On the left, the raw image; on the right, the processed image after performing a *ToT* selection and removing non-point-like clusters.



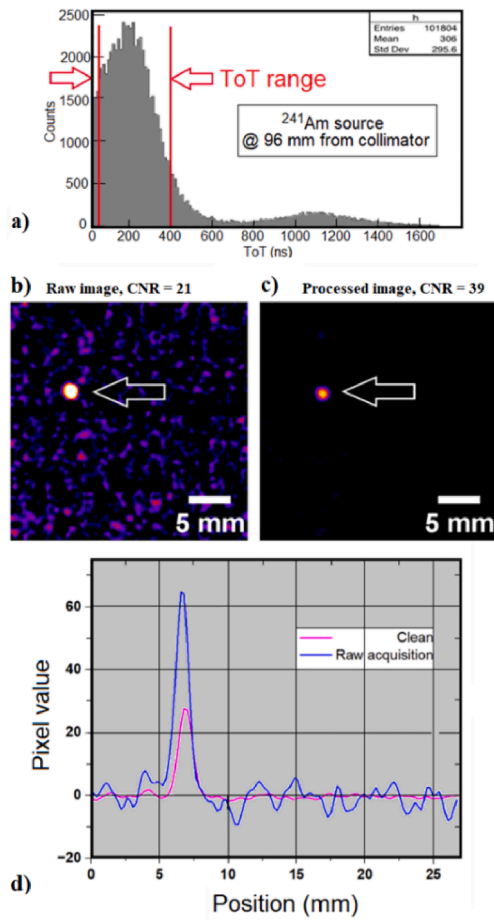


**Fig. 12.** a) Histogram of the tot pixel value of the events revealed for a  $^{241}\text{Am}$  source placed at 96 mm from the collimator. b) Reconstructed image of the source (reconstructed object plane at 98 mm from the collimator) after applying a Gaussian filter (sigma = 1 pixel). The white arrow indicates the source. c) Reconstructed image of the  $^{241}\text{Am}$  source after applying the ToT selection and a Gaussian spatial filter (sigma = 1 pixel). d) A line profile across the source images b) and c) shows that the ToT windowing permitted to increase the CNR (by 86%).

It then decreases due to “defocusing”, so producing a peak in the CNR vs source-collimator distance curve (Fig. 9). The axial spatial resolution can be estimated as the FWHM of the Gaussian fit of the CNR peak. In Fig. 9a we determined a value of 9.4 mm FWHM (at 62 mm source-collimator distance). The FWHM axial spatial resolution was also assessed from the MC simulation (Fig. 9b) and compared to the one obtained from the experimental test (Fig. 9a). While for the latter it was found to be  $9.4 \pm 0.5$  mm, from the MC simulation this resolution was  $8.2 \pm 0.2$  mm: the agreement between these two values is considered a reasonable validation of MC simulation prediction of the performance of the CA mask.

In-focus images obtained from experimental tests were compared with those obtained from MC, as shown in Fig. 10. The FOV of the CA mask was  $19.22 \times 19.22$  mm<sup>2</sup> in both images (experiment, Fig. 17a, and simulation, Fig. 10b), in agreement with CA mask theory. The CNR of the sources evaluated for the two images (for a circular ROI of 12 pixels area) were comparable (Fig. 10c), the profiles of the sources being quite similar.

### 3.2. Experimental tests and MC simulation for a $^{241}\text{Am}$ source

Fig. 11 shows the acquired (a) and processed (b) images obtained with a  $^{241}\text{Am}$  source placed at 96 mm from the CA collimator. The cleaning procedure included both the clustering analysis (to exclude any

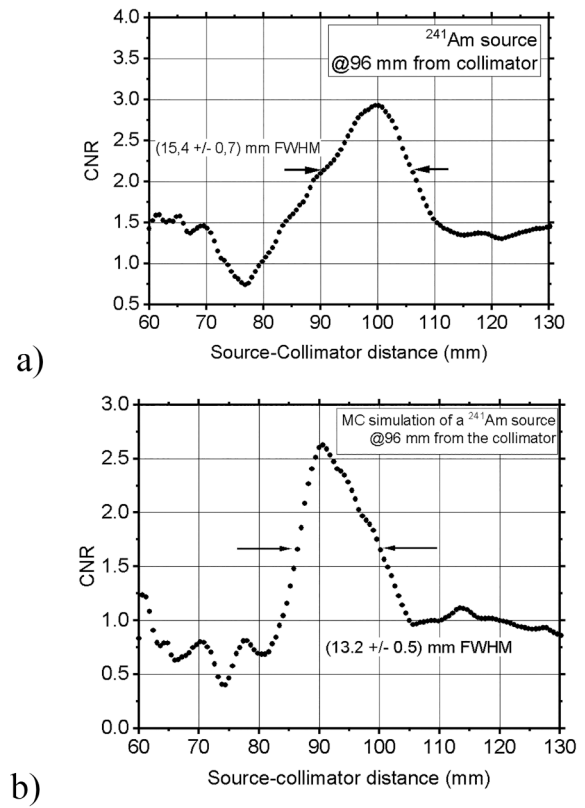


**Fig. 13.** a) CNR vs source-collimator distance for the experimentally obtained image of the  $^{241}\text{Am}$  source placed at 96 mm from the collimator. The axial resolution was 15.4 mm FWHM. b) Corresponding axial profile obtained from MC simulations showed an axial resolution of 13.2 mm FWHM.

non-pointy cluster) and a selection of the ToT of the events; in this case, we selected events having a ToT between 50 ns and 400 ns (Fig. 12a).

The experimental assessment of the axial resolution for the  $^{241}\text{Am}$  source produced a value of  $15.4 \pm 0.7$  mm FWHM (Fig. 13a). As we did for the  $^{133}\text{Ba}$  source, we performed a MC simulation to reproduce the experimental setup with the  $^{241}\text{Am}$  source; the value of the axial resolution derived from MC simulations  $13.2 \pm 0.5$  mm FWHM was in reasonable agreement with the experimental result. In-focus images of experimental and simulated tests are shown in Fig. 14. This figure confirms the good visual agreement between the experiment and the simulation, once we consider the low statistics (high noise) of the MC simulation.

### 3.3. Field of view of the newly designed CA mask

Fig. 15 shows the output images for a simulated  $^{99\text{m}}\text{Tc}$  point-like source placed at the center of the FOV, at 50 mm from the collimator face, with air between the source and the collimator. The raw simulated image is reported in Fig. 15a and the corresponding decoded image is in Fig. 15b and 15c. The CNR evaluated in this case was  $\approx 40$ .

For decoded images of point-like sources placed at several points in the FOV of the mask at 50 mm axial distance from the collimator face, the CNR was between 10 and 45 for all source positions up to 2 mm from the border of the FOV (90.3 mm by side); CNR decreases linearly as the lateral distance from the collimator axis increases (Fig. 16). This indicated image quality degradation for off-axis sources, due to decreasing geometric efficiency.

From a series of MC simulations with a point-like  $^{99\text{m}}\text{Tc}$  source placed off-axis, we determined at 50 mm source-collimator distance, the useful FOV has an extent of about 88 mm, in good agreement with the value (90.3 mm) predicted by CA imaging theory.

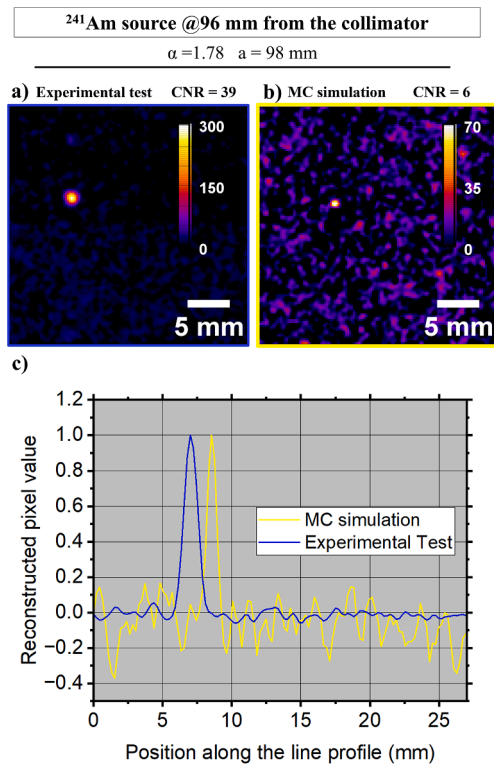


**Fig. 14.** a) Image of the  $^{241}\text{Am}$  source (placed at 96 mm from the collimator) obtained from experimental tests. b) Reconstructed image of the simulated source (object plane at 98 mm). c) Source line profile for the measured (blue) and simulated (yellow) images, normalized to their maximum value.

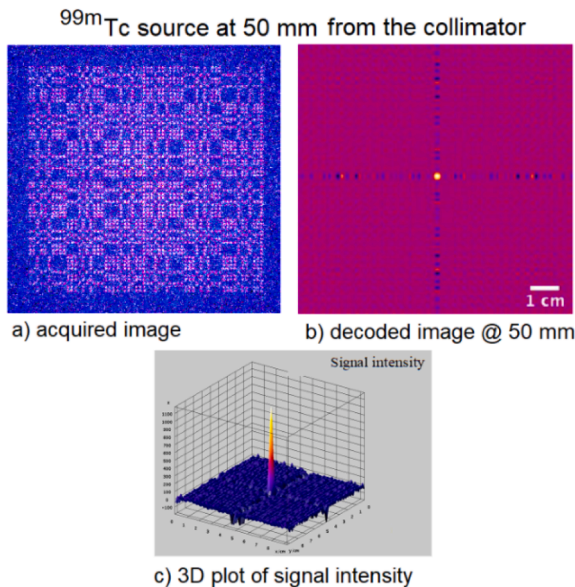


**Fig. 15.** Output images (in false color scale) of the MC simulation of a point-like  $^{99\text{m}}\text{Tc}$  source placed on-axis at 50 mm distance from the collimator, emitting  $10^7$  photons onto the detector area. a) Image (number of detected photons per detector pixel) acquired by the simulated detector (1 mm thick CdTe), where the projection of the mask onto the detector area is evident; b) decoded image, showing the reconstructed source at the center of the image, as well as cross-like artifacts arising in the decoding process; c) 3D surface plot of the decoded image shown in b), indicating high detail contrast above noise.

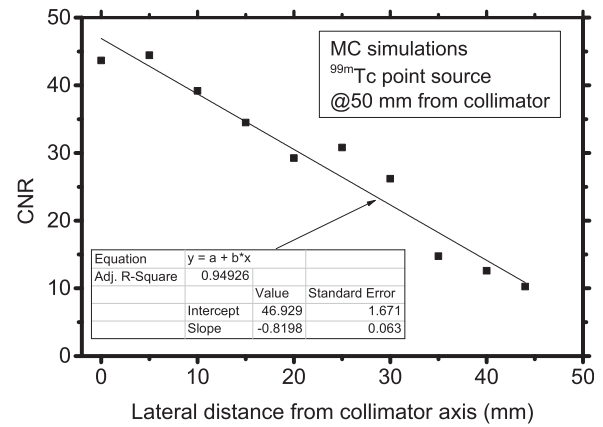


**Fig. 16.** CNR (data points) evaluated from decoded images of MC simulations, as a function of the lateral distance from the axis of the collimator. CNR was assessed in successive simulations in which a  $^{99\text{m}}\text{Tc}$  point-like source was placed on an object plane at 50 mm from the collimator face, at various lateral distances from the FOV center. A linear fit shows decreasing image quality for point-like source positions approaching the border of the FOV.

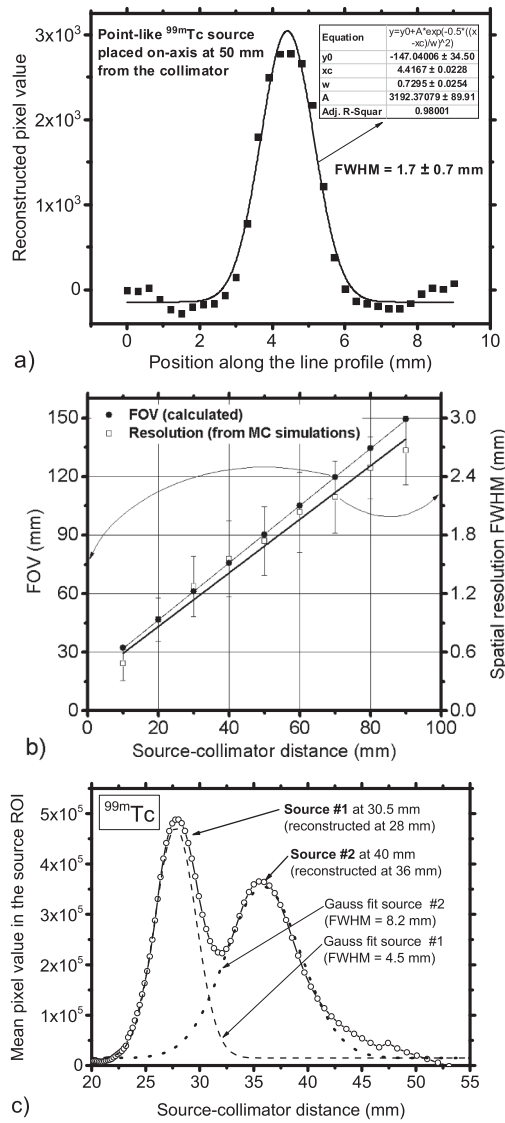
#### 3.4. Lateral and axial spatial resolutions for the newly designed MediPROBE4 camera

Fig. 17a shows the Gaussian fit performed on the line profile across the MC-simulated and reconstructed image of an axial point-like  $^{99\text{m}}\text{Tc}$  source, at 50 mm from the collimator face. From this profile, we computed the lateral spatial resolution of the collimator, which was  $1.7 \pm 0.7$  mm FWHM. After summing the detector resolution in quadrature (assumed to be  $110 \mu\text{m}$ , i.e., 2 pixels), the system spatial resolution was  $1.7 \pm 0.7$  mm FWHM (at 50 mm distance from the collimator, where the calculated FOV is 90 mm by side). Fig. 17b shows the spatial resolution as a function of the source-collimator distance, as determined from a series of MC simulations with point-like  $^{99\text{m}}\text{Tc}$  sources placed at various distances from the collimator. The corresponding image FOV is plotted, from which a trade-off can be determined between lateral resolution and FOV. Fig. 17c shows the CNR of two point-like  $^{99\text{m}}\text{Tc}$  sources, calculated for circular ROIs of 21 pixels area (from images reconstructed in two MC simulations), as a function of the source-collimator axial distance, for two sources placed on-axis. The sources were separated by 6.5 mm (proximal source at 30.5 mm and distal source at 40.0 mm axial distance from the collimator). In this plot, the axial location of these two sources can be identified as two well-separated peaks, with a maximum absolute discrepancy of 3 mm in depth. By fitting each peak with a Gaussian curve, one can derive the axial (longitudinal) spatial resolution based on CNR assessment, which is 8.2 mm FWHM at 40 mm from the collimator face, and 4.5 mm FWHM at 30.5 mm axial distance (Fig. 17c).

#### 3.5. Sensitivity of the newly designed MediPROBE4 camera

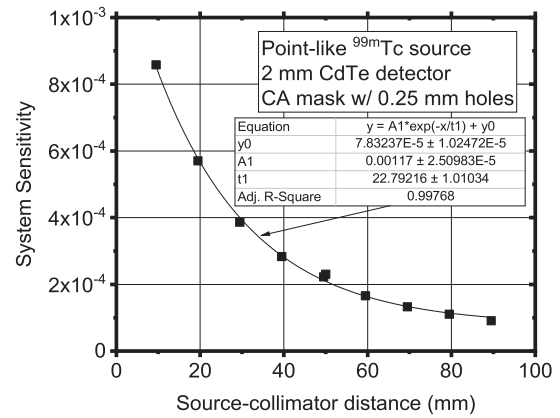
The photopeak intrinsic detection efficiency estimated from MC simulations was  $29.1 \pm 1.9$  % for a 1-mm thick CdTe detector, and  $50.1 \pm 1.3$  % for a 2 mm thick detector (selecting a minimum detection threshold of 60 keV). The fluorescence events represent 2.2% and 6.1% of the total hits, for 1 mm and 2 mm detectors, respectively. For a source placed axially at 50 mm from the collimator face, the background subtracted geometrical sensitivity of the collimator is  $4 \times 10^{-4}$ . Considering the detection efficiency and the geometrical sensitivity, for a source placed at 50 mm from the collimator face, the expected system sensitivity for a 1 mm thick CdTe sensor is  $1.2 \times 10^{-4}$ , and of  $2.2 \times 10^{-4}$  for a 2 mm thick detector.

Fig. 18 shows the system sensitivity of the CA mask, as a function of the source-collimator distance. In the MC simulation, we considered a 2-



**Fig. 17.** a) Source profile along a horizontal line in Fig. 15, for a point-like  $^{99m}\text{Tc}$  source placed on axis at 50 mm from the collimator (data points). Two Gaussian fits are shown for the profile of the sources (lines), from which the lateral spatial resolution is derived, as  $1.7 \pm 0.7$  mm FWHM. b) Lateral spatial resolution determined from MC simulations, and side of the image FOV, as a function of the distance from the collimator. Linear fits on the data have been drawn. c) CNR as a function of the distance from the collimator (data points), for two simulated point-like sources placed on-axis, at 30.5 mm and 40 mm from the collimator, respectively. Gaussian fits of the two peaks show centroid and FWHM value of the two reconstructed source profiles.

mm thick CdTe detector. A similar simulation was carried out for a single hole (channel pinhole) in this mask, which indicated that at 50 mm source distance the estimated system sensitivity corresponds to 0.022 cps/kBq, i.e., 292 times that for a single 0.25 mm aperture pinhole. This axial sensitivity is equivalent to that of a single knife-edge pinhole with an aperture diameter of 4.25 mm. The functional decrease of sensitivity vs. source distance from the collimator (Fig. 18) is a combined result of i) a decrease of source intensity with the inverse square of the distance; ii) an increasing geometric efficiency of the CA mask at increasing distances of the source when multiple apertures “see” the source; and iii) a limited acceptance angle of the channel pinhole aperture ( $28^\circ$ ).



**Fig. 18.** System sensitivity as a function of source-collimator distance, estimated from MC simulations using background-subtracted sensitivity for the CA mask (0.25 mm hole apertures) and detection efficiency of a 2 mm thick CdTe detector. An exponential function well fits the data. At 50 mm from the collimator, the sensitivity is 292 times larger than that of a single hole in the CA mask.

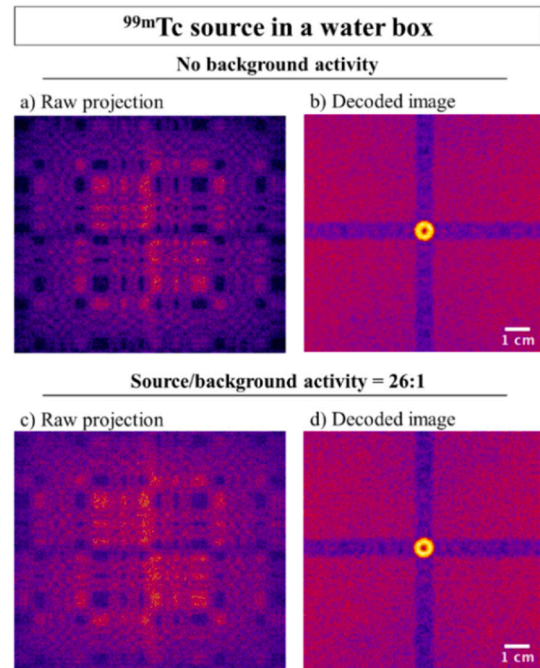


**Fig. 19.** a) False color projection images of the mask onto a  $448 \times 512$  pixel detector, for a spherical source (10 mm diameter) placed in a water box of  $90 \times 90 \times 50$  mm<sup>3</sup> simulating the embedding soft tissue, and b) corresponding decoded image. c) In this projected image the water box contains a uniform background activity with an SBR = 26:1; d) corresponding decoded image.

### 3.6. Image of a spherical source in a water box using the newly designed CA mask

MC simulations of a spherical source placed within a water box (Fig. 19a,b) showed a significant reduction in the CNR with respect to a point-like source in air; nevertheless, the image quality is still sufficient to visualize the source. With the addition of background activity (Fig. 19c,d), the CNR further decreases from 6.95 (Fig. 19b) to 5.45 (Fig. 19d).



**Table 4**

Performance of some commercial and experimental CGCs. MediPROBE2 was equipped with a 1-mm thick CdTe detector.

CGC [Ref.]	Field of view (mm <sup>2</sup> ) @50 mm	System spatial resolution (mm) @50 mm	Sensitivity (cps/kBq)
MediPROBE2 (0.94 mm pinhole) [16]	70.4 × 70.4	5.5	6.5 × 10 <sup>-3</sup> @ 50 mm
MediPROBE2 (1.9 mm pinhole) [35]	28 × 28	5.0	4.9 × 10 <sup>-2</sup> @ 50 mm
MediPROBE2 (0.08 mm CA mask) [16]	40 × 40	0.64 ± 5%	5.9 × 10 <sup>-2</sup> @50 mm
eZ SCOPE [30]	32 × 32	7.9	1.8 × 10 <sup>-4</sup> @0 mm
POCI [31]	40 mm in diameter	7.6	1.9 × 10 <sup>-1</sup> @50 mm
CGC [36]	40 × 40	2.9	2.1 × 10 <sup>-1</sup> @3 mm
Sentinella 102® [32–34] 2.5 mm pinhole collimator	67 × 67 (interpolated)	7.3	5.0 × 10 <sup>-1</sup> @50 mm
MediPROBE4 (0.25 mm CA mask) (2-mm CdTe)	88 × 88	1.7 ± 0.7	2.2 × 10 <sup>-1</sup> @50 mm

#### 4. Discussion

The above preliminary assessment of the performance of MediPROBE4, carried out via MC simulations and experimental tests, produced a picture of the characteristics of the new CGC, which in Table 4 are compared with those of some present commercial and experimental CGCs. For further comparisons among state-of-the-art CGCs, a comprehensive review of compact gamma cameras in the last decade has appeared recently [37].

With respect to the previous probe (MediPROBE2) utilizing a Timepix2 with a CdTe (1 mm thick) detector and a CA mask (0.08 mm aperture), the major advancements here shown are the increase of the Timepix4 detector sensitive area (from about 2 cm<sup>2</sup> to about 7 cm<sup>2</sup>), and to the use of a more efficient CA collimator (0.25 mm aperture). As expected, these changes decrease the spatial resolution (from 0.64 mm to 1.7 mm at 50 mm distance), but correspondingly, the useful FOV and the system sensitivity increase significantly (Table 4). With respect to using MediPROBE2 with a photon counting detector (Medipix2 ASIC), Timepix4 allows energy sensitive detection of the energy of the interacting photon; with respect to MediPROBE2 using a Timepix2 ASIC, MediPROBE4 features a larger detector area which produced the above high performance in terms of sensitivity, resolution and FOV.

As for all Timepix series ASICs, the ToA feature of Timepix4 allows to recognize the cluster of pixels hit by a single photon, necessary to overcome the charge-sharing problem and to also permit discrimination of multiple radiation sources [38].

With respect to a scintillator-based commercial CGC (Sentinella 102® by Oncovision, Valencia, Spain), which is twice as sensitive at 50 mm distance from the collimator, MediPROBE4 equipped with a 2-mm thick CdTe detector is predicted to feature a better spatial resolution (1.7 mm vs. 7.3 mm) at a relatively larger FOV (88 × 88 mm<sup>2</sup> vs. 67 × 67 mm<sup>2</sup> estimated) (Table 4).

#### 5. Conclusions

We presented a layout of the new CGC MediPROBE4 based on the Timepix4 hybrid pixel detector, as well as MC simulations and first experimental tests of its performance with laboratory radioactive sources. 3D spectral images of gamma-ray radioactive sources (<sup>241</sup>Am and <sup>133</sup>Ba) were obtained. Once equipped with a 2-mm thick CdTe pixel detector, and a CA mask with 0.25 mm apertures, MediPROBE4 characteristics appear promising in view of its future realization with 2-mm thick CdTe detectors, and validation in a clinical environment. By

comparing results from our MC simulations with the experimental tests, we demonstrated that our simulation platform can predict the imaging performance of the CGC we designed. The Geant4-based code could also simulate similar devices by setting the relative geometrical and constructive parameters.

#### Declaration of Competing Interest

The authors declare that they have no known competing financial interests or personal relationships that could have appeared to influence the work reported in this paper.

#### Acknowledgments

The coded aperture mask reconstruction software was written and kindly provided by Dr. R. Accorsi when at MIT, Cambridge, MA, USA. The coded aperture masks used in the experimental tests were realized within a collaboration with R. Lanza and R. Accorsi (MIT). The Timepix4 ASIC has been developed within the Medipix4 collaboration (<https://medipix.web.cern.ch/medipix4>). This work was supported by INFN, Italy, within the projects Medipix4 and MC-INFN.

#### References

- [1] Heller S, Zanzonico P. Nuclear probes and intraoperative gamma cameras. *Semin Nucl Med* 2011;41:166–81. <https://doi.org/10.1053/j.semnucmed.2010.12.004>.
- [2] Fujii T, Yamaguchi S, Yajima R, Tsutsumi S, Uchida N, Asao T, et al. Use of a Handheld, Semiconductor (Cadmium Zinc Telluride)-Based Gamma Camera in Navigation Surgery for Primary Hyperparathyroidism. *Am Surg* 2011;77:690–3. <https://doi.org/10.1177/000313481107700621>.
- [3] Pani R, Guidoccio F, Scafe R, Zanzonico P, Mariani G. In: General-Purpose Gamma Cameras, Dedicated Gamma Cameras, and Gamma-Probes for Radioguided Surgery. *Nuclear Medicine Textbook*. Springer International Publishing; 2019. p. 137–71. [https://doi.org/10.1007/978-3-319-95564-3\\_6](https://doi.org/10.1007/978-3-319-95564-3_6).
- [4] Tsuchimochi M, Hayama K. Intraoperative gamma cameras for radioguided surgery: Technical characteristics, performance parameters, and clinical applications. *Phys Med* 2013;29:126–38. <https://doi.org/10.1016/j.ejpm.2012.05.002>.
- [5] Russo P, Mettievier G, Pani R, Pellegrini R, Cinti MN, Bennati P. Imaging performance comparison between a LaBr<sub>3</sub>:Ce scintillator based and a CdTe semiconductor based photon counting compact gamma camera. *Med Phys* 2009;36:1298–317. <https://doi.org/10.1118/1.3081412>.
- [6] Esposito M, Jakubek J, Mettievier G, Pospisil S, Russo P, Solc J. Energy sensitive Timepix silicon detector for electron imaging. *Nucl Instrum Methods Phys Res A* 2011;652:458–61. <https://doi.org/10.1016/j.nima.2011.01.148>.
- [7] Lauria A, Mettievier G, Montesi MC, Aloj L, Lastoria S, Aurilio M, et al. Experimental study for an intraoperative probe for 18F imaging with a silicon pixel detector. *Nucl Instrum Methods Phys Res A* 2007;576:198–203. <https://doi.org/10.1016/j.nima.2007.01.152>.
- [8] Autiero M, Celentano L, Cozzolino R, Laccetti P, Marotta M, Mettievier G, et al. Experimental study on in vivo optical and radionuclide imaging in small animals. *IEEE Trans Nucl Sci* 2005;52:205–9. <https://doi.org/10.1109/TNS.2004.843095>.
- [9] Accorsi R, Autiero M, Celentano L, Chmeissani M, Cozzolino R, Curion AS, et al. MediSPECT. Single photon emission computed tomography system for small field of view small animal imaging based on a CdTe hybrid pixel detector. *Nucl Instrum Methods Phys Res A* 2007;571:44–7. <https://doi.org/10.1016/j.nima.2006.10.025>.
- [10] Accorsi R, Curion AS, Frallicciardi P, Lanza RC, Lauria A, Mettievier G, et al. Preliminary evaluation of the tomographic performance of the mediSPECT small animal imaging system. *Nucl Instrum Methods Phys Res A* 2007;571:415–8. <https://doi.org/10.1016/j.nima.2006.10.123>.
- [11] Bertolucci E, Maiorino M, Mettievier G, Montesi MC, Russo P. Preliminary test of an imaging probe for nuclear medicine using hybrid pixel detectors. *Nucl Instrum Methods Phys Res A* 2002;487(1–2):193–201. [https://doi.org/10.1016/S0168-9002\(02\)00965-8](https://doi.org/10.1016/S0168-9002(02)00965-8).
- [12] Mettievier G, Montesi MC, Russo P. Design of a compact gamma camera with semiconductor hybrid pixel detectors: Imaging tests with a pinhole collimator. *Nucl Instrum Methods Phys Res A* 2003;509:321–7. [https://doi.org/10.1016/S0168-9002\(03\)01644-9](https://doi.org/10.1016/S0168-9002(03)01644-9).
- [13] Chmeissani M, Frojdh C, Gal O, Llopert X, Ludwig J, Maiorino M, et al. First experimental tests with a CdTe photon counting pixel detector hybridized with a Medipix2 readout chip. *IEEE Trans Nucl Sci* 2004;51:2379–85. <https://doi.org/10.1109/TNS.2004.832324>.
- [14] Russo P, Curion AS, Mettievier G, Esposito M, Aurilio M, Caracò C, et al. Evaluation of a CdTe semiconductor based compact gamma camera for sentinel lymph node imaging. *Med Phys* 2011;38:1547–60. <https://doi.org/10.1118/1.3555034>.
- [15] Llopert X, Campbell M, San Segundo D, Pernigotti E, Dinapoli R. Medipix2, a 64k pixel read out chip with 55 μm square elements working in single photon counting mode. 2001 IEEE Nuclear Science Symposium Conference Record (Cat.

- No.01CH37310), San Diego, CA, USA: IEEE; 2001. p. 1484–8. <https://doi.org/10.1109/NSSMIC.2001.1008618>.
- [16] Russo P, Di Lillo F, Corvino V, Frallicciardi PM, Sarno A, Mettievier G. CdTe compact gamma camera for coded aperture imaging in radioguided surgery. *Phys Med* 2020;69:223–32. <https://doi.org/10.1016/j.ejmp.2019.12.024>.
- [17] Accorsi R, Gasparini F, Lanza RC. Optimal coded aperture patterns for improved SNR in nuclear medicine imaging. *Nucl Instrum Methods Phys Res A* 2001;474(3): 273–84. [https://doi.org/10.1016/S0168-9002\(01\)01326-2](https://doi.org/10.1016/S0168-9002(01)01326-2).
- [18] Accorsi R, Celentano L, Laccetti P, Lanza RC, Marotta M, Mettievier G, et al. High-resolution 125i small animal imaging with a coded aperture and a hybrid pixel detector. *IEEE Trans Nucl Sci* 2008;55:481–90. <https://doi.org/10.1109/TNS.2007.909846>.
- [19] Schellingerhout D, Accorsi R, Mahmood U, Idoine J, Lanza RC, Weissleder R. Coded Aperture Nuclear Scintigraphy: A Novel Small Animal Imaging Technique. *Mol Imaging* 2002;1:344–53. <https://doi.org/10.1162/1535350020022136>.
- [20] Mok GSP, Wang Y, Tsui BMW. Quantification of the multiplexing effects in multipinhole small animal SPECT: A simulation study. *IEEE Trans Nucl Sci* 2009;56: 2636–43. <https://doi.org/10.1109/TNS.2009.2023444>.
- [21] Gottesman SR, Fenimore EE. New family of binary arrays for coded aperture imaging. *Appl Opt* 1989;28:4344. <https://doi.org/10.1364/ao.28.004344>.
- [22] Fujii H, Idoine JD, Gioux S, Accorsi R, Slochower DR, Lanza RC, et al. Optimization of coded aperture radioscinigraphy for sentinel lymph node mapping. *Mol Imaging Biol* 2012;14:173–82. <https://doi.org/10.1007/s11307-011-0494-2>.
- [23] Russo P, Mettievier G. Method for measuring the focal spot size of an x-ray tube using a coded aperture mask and a digital detector. *Med Phys* 2011;38:2099–115. <https://doi.org/10.1118/1.3567503>.
- [24] Llopart X, Alozy J, Ballabriga R, Campbell M, Casanova R, Gromov V, et al. Timepix4, a large area pixel detector readout chip which can be tiled on 4 sides providing sub-200 ps timestamp binning. *J Instrum* 2022;17. <https://doi.org/10.1088/1748-0221/17/01/C01044>. IOP Publishing Ltd.
- [25] Ballabriga R, Alozy JA, Bandi FN, Blaj G, Campbell M, Christodoulou P, et al. The Timepix4 analog front-end design: Lessons learnt on fundamental limits to noise and time resolution in highly segmented hybrid pixel detectors. *Nucl Instrum Methods Phys Res A* 2023;1045:167489. <https://doi.org/10.1016/j.nima.2022.167489>.
- [26] Ballabriga R, Campbell M, Llopart X. Asic developments for radiation imaging applications: The medipix and timepix family. *Nucl Instrum Methods Phys Res A* 2018;878:10–23. <https://doi.org/10.1016/j.nima.2017.07.029>.
- [27] Heijden B Van Der, Visser J, Beuzekom M Van, Boterenbrood H, Kulis S, Munneke B, et al. SPIDR, a general-purpose readout system for pixel ASICs. *J Instrum* 2017;12:C02040. <https://doi.org/10.1088/1748-0221/12/02/C02040>.
- [28] CERN. Geant4 simulation toolkit 2022. <https://geant4.web.cern.ch/> (accessed June 1, 2022).
- [29] Bolzonella R. Timepix4 Data Analysis Tool 2022. <https://baltig.infn.it/medipix4/medipix4-data-analysis-tools> (accessed June 1, 2022).
- [30] Abe A, Takahashi N, Lee J, Oka T, Shizukuishi K, Kikuchi T, et al. Performance evaluation of a hand-held, semiconductor (CdZnTe)-based gamma camera. *Eur J Nucl Med Mol Imaging* 2003;30:805–11. <https://doi.org/10.1007/s00259-002-1067-z>.
- [31] Pitre S, Ménard L, Ricard M, Solal M, Garbay JR, Charon Y. A hand-held imaging probe for radio-guided surgery: Physical performance and preliminary clinical experience. *Eur J Nucl Med Mol Imaging* 2003;30:339–43. <https://doi.org/10.1007/s00259-002-1064-2>.
- [32] Sánchez F, Fernández MM, Giménez M, Benlloch JM, Rodríguez-Alvarez MJ, García De Quirós F, et al. Performance tests of two portable mini gamma cameras for medical applications. *Med Phys* 2006;33:4210–20. <https://doi.org/10.1118/1.2358199>.
- [33] Food and Drug Administration. FDA. FDA Summary: Portable Gamma Camera: Sentinella 102 GEM-IMAGING SA. 2009. [https://www.accessdata.fda.gov/cdrh\\_docs/pdf9/K092471.pdf](https://www.accessdata.fda.gov/cdrh_docs/pdf9/K092471.pdf).
- [34] Riccardi L, Gabusi M, Bignotto M, Gregianin M, Vecchiato A, Paiusco M. Assessing good operating conditions for intraoperative imaging of melanoma sentinel nodes by a portable gamma camera. *Phys Med* 2015;31:92–7. <https://doi.org/10.1016/j.ejmp.2014.10.079>.
- [35] Acampa W, Capussella T, Cuocolo A, Di Lillo F, Punzo G, Quarto M, et al. Characterization of a small FOV portable GC: MediPROBE. *Radiat Prot Dosimetry* 2019;183:290–6. <https://doi.org/10.1093/rpd/ncy229>.
- [36] Bugby SL, Lees JE, Bhatia BS, Perkins AC. Characterisation of a high resolution small field of view portable gamma camera. *Phys Med* 2014;30:331–9. <https://doi.org/10.1016/j.ejmp.2013.10.004>.
- [37] Farnworth AL, Bugby SL. Intraoperative Gamma Cameras: A Review of Development in the Last Decade and Future Outlook. *J Imaging* 2023;9. <https://doi.org/10.3390/jimaging9050102>.
- [38] Solc J, Jakubek J, Marek L, Oancea C, Pivec J, Šmolodasová J, et al. Monte Carlo modelling of pixel clusters in Timepix detectors using the MCNP code. *Phys Med* 2022;101:79–86. <https://doi.org/10.1016/j.ejmp.2022.08.002>.